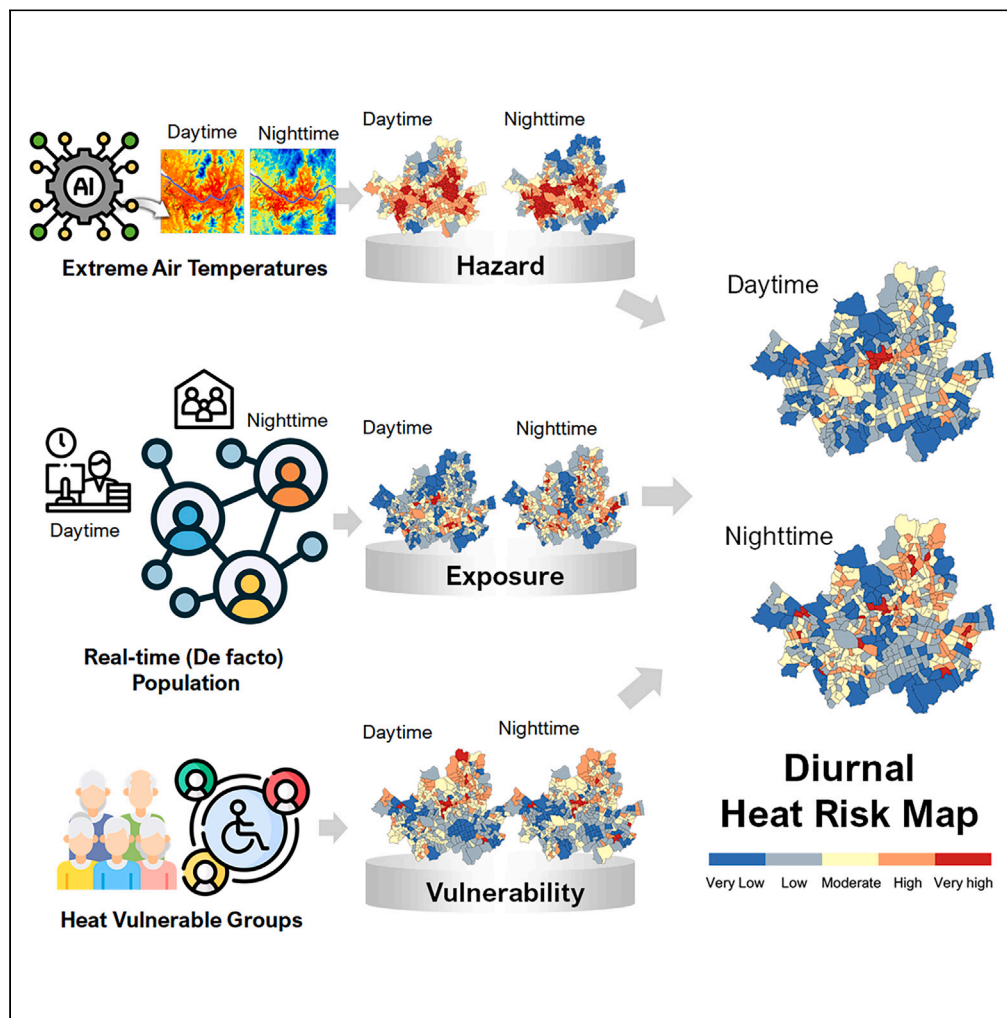


Article

# Diurnal urban heat risk assessment using extreme air temperatures and real-time population data in Seoul



Cheolhee Yoo,  
Jungho Im, Qihao  
Weng, Dongjin  
Cho, Eunjin Kang,  
Yeji Shin

ersgis@unist.ac.kr (J.I.)  
qihao.weng@polyu.edu.hk  
(Q.W.)

**Highlights**

Machine-learning-based  
air temperature analysis  
revealed daily heat hazard  
variations

Real-time population data  
are essential for accurate  
diurnal heat risk maps

Daytime heat risk exhibited  
stronger correlations with  
heat illness ratios than  
nighttime



## Article

## Diurnal urban heat risk assessment using extreme air temperatures and real-time population data in Seoul

Cheolhee Yoo,<sup>1,2</sup> Jungho Im,<sup>3,5,\*</sup> Qihao Weng,<sup>1,2,\*</sup> Dongjin Cho,<sup>3</sup> Eunjin Kang,<sup>3</sup> and Yeji Shin<sup>3,4</sup>

## SUMMARY

Previous heat risk assessments have limitations in obtaining accurate heat hazard sources and capturing population distributions, which change over time. This study proposes a diurnal heat risk assessment framework incorporating spatiotemporal air temperature and real-time population data. Daytime and nighttime heat risk maps were generated using hazard, exposure, and vulnerability components in Seoul during the summer of 2018. The hazard was derived from the daily extreme air temperatures obtained using the stacking machine learning model. Exposure was calculated using *de facto* population density, and vulnerability was assessed using demographic and socioeconomic indicators. The resulting maps revealed distinct diurnal spatial patterns, with high-risk areas in the urban core during the day and dispersed at night. Daytime heat risk was strongly correlated with heat-related illness ratios ( $R = 0.8$ ) and accurately captured temporal fluctuations in heat-related illness incidence. The proposed framework can guide site-specific adaptation and response plans for dynamic urban heat events.

## INTRODUCTION

Globally, the occurrence, severity, and duration of heat waves are on an unmistakable upward trend, and are projected to intensify significantly during the forthcoming century according to climate change scenarios.<sup>1–3</sup> Numerous investigations have emphasized that these extreme thermal events trigger a substantial surge in heat-related fatalities, especially in urban areas.<sup>4–6</sup> Unfortunately, most cities worldwide are unprepared to address the impending risks associated with extreme heat.<sup>7</sup>

To formulate effective policies and devise location-specific plans for adapting to and responding to heat waves, scientists and planners must understand the spatiotemporal dynamics of extreme heat risk. This involves understanding three key elements<sup>8</sup>: hazard (the frequency and intensity of extreme temperatures), exposure (the magnitude of an individual's or population's contact with a risk source), and vulnerability (a specific population group's inability to tolerate the consequences of a hazardous environment).

The use of heat hazard sources in previous heat risk assessments had several limitations. Numerous studies have used land surface temperature (LST) data, retrieved from thermal infrared remote sensing as hazard sources.<sup>9–11</sup> However, LST is limited because of the trade-off between spatial and temporal resolutions, which is an obstacle to acquiring high spatiotemporal temperature data.<sup>12</sup> In addition, satellite LST cannot be obtained under cloudy conditions, which can cause difficulties in the timely identification of extreme summer heat events. It is important to note that LST differs from air temperature, particularly on urban surfaces.<sup>13</sup> Because humans perceive temperatures approximately 1.5–2 m above the ground, air temperature is a more appropriate hazard source than LST. Nevertheless, the number of weather stations that provide air temperature data within a city is often insufficient to capture the thermal heterogeneity of complex urban landscapes.<sup>14</sup>

To calculate exposure and vulnerability, most studies use demographic data based on place of residence.<sup>10,11,15–17</sup> In cities, however, the spatial distribution of the resident population (the *de jure* population, the number of people officially registered as inhabitants of a given area) differs from that of the actual real-time population (the *de facto* population, all people recorded at the time of measurement in a given area) because of numerous socioeconomic and leisure activities, especially during daytime. Thus, if we evaluate risk based on the *de jure* population, the spatial distribution of heat risk cannot accurately reflect the actual exposure or identify the vulnerable groups.

While key components of heat risk—notably hazard and exposure—exhibit daily or hourly variation, many previous studies have used yearly data as the target temporal scale for heat risk maps.<sup>10,11,18,19</sup> In addition, few studies have mapped the heat risk separately for day and night.<sup>10</sup> However, the spatial temperature distributions and population activities within a city change over time.<sup>20,21</sup> For instance, building

<sup>1</sup>JC STEM Lab of Earth Observations, Department of Land Surveying and Geo-Informatics, The Hong Kong Polytechnic University, Hung Hom, Hong Kong

<sup>2</sup>Research Centre for Artificial Intelligence in Geomatics, The Hong Kong Polytechnic University, Hung Hom, Hong Kong

<sup>3</sup>Department of Civil, Urban, Earth, and Environmental Engineering, Ulsan National Institute of Science and Technology (UNIST), Ulsan, South Korea

<sup>4</sup>Market Intelligence Team, Purchasing Strategy Unit, CJ CheilJedang Corporation, Market Intelligence Team, Seoul, South Korea

<sup>5</sup>Lead contact

\*Correspondence: [ersgis@unist.ac.kr](mailto:ersgis@unist.ac.kr) (J.I.), [qihao.weng@polyu.edu.hk](mailto:qihao.weng@polyu.edu.hk) (Q.W.)

<https://doi.org/10.1016/j.isci.2023.108123>



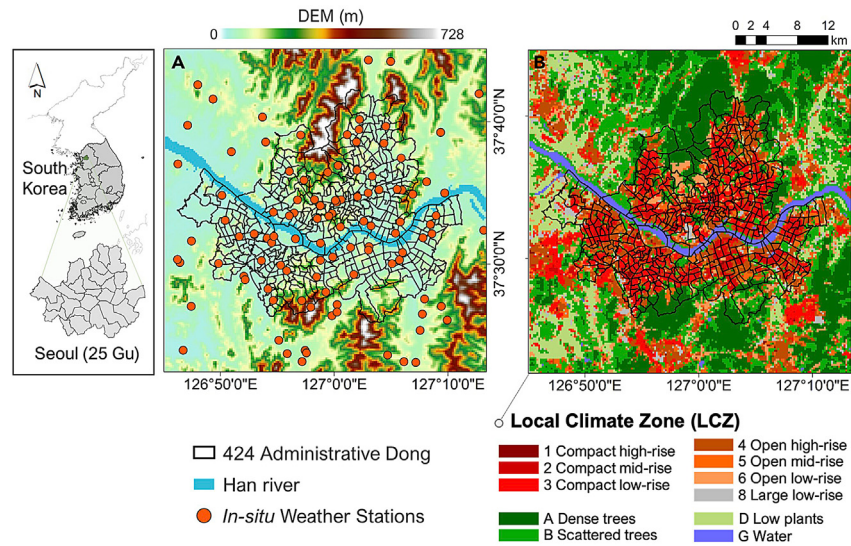


**Figure 1. Study area and Local Climate Zone (LCZ) map of Seoul**

(A) Location of weather stations in Seoul. Background elevation was obtained from the Shuttle Radar Topography Mission (SRTM) digital elevation model (DEM) with a spatial resolution of 250 m.

(B) The background layer is the 250 m resolution local climate zone (LCZ), which is a standardized classification system that represents the characteristics of urban forms and functions.<sup>25</sup> The LCZ maps for the three cities were adopted from Yoo et al.<sup>28</sup>

materials in urban areas retain heat longer than vegetation,<sup>22</sup> resulting in distinct daytime and nighttime thermal spatial distributions.<sup>23</sup> Similarly, population activities vary; people often commute from homes to workplaces or schools during the day and stay in residential areas at night. These patterns further differ between weekdays and weekends.<sup>24</sup> Therefore, daily heat risk assessments at different times in urban areas are vital to help local governments understand the temporal variation in risk and analyze hotspots in detail for specific times, such as extreme heat events. Consideration of temporal variations in thermal characteristics can allow for realistic and cost-effective action plans in response to heat risks.

The development of a new heat risk assessment framework, aimed at addressing existing challenges, raises several crucial research questions.

- **Air temperature-based heat hazard:** Can we construct an accurate, spatially continuous daily air temperature map in urban areas for heat hazard assessment, thereby enabling the examination of differences in the spatial and temporal variations of daytime and nighttime hazards?
- **De facto population-based heat exposure:** How does a heat exposure map constructed using *de facto* population data compare in spatiotemporal distribution with one created using *de jure* population data?
- **Diurnal heat risk map:** Can a heat risk map developed based on daily fluctuations in factors such as air temperature and *de facto* population effectively represent the risk of heat-related illnesses?

This study focused on Seoul, South Korea. The target spatial scale for the risk map was the *dong*, the sub-municipal-level administrative unit of the city. We concentrate on the summer season (July–August) of 2018 in Seoul, which was characterized by an unprecedented heat-wave of an unusually prolonged duration. The objectives of this research were to (1) develop a framework for mapping daily heat risk in the daytime and nighttime using indicators closer to reality; (2) analyze the spatial distribution and temporal trends of hazard, exposure, and vulnerability during the daytime and nighttime; (3) assess the daily heat risk during both daytime and nighttime in Seoul at the *dong* unit level and investigate the hotspots of severe heat risk in the city; and (4) validate the produced risk map using heat-related illness data.

## RESULTS

### Air temperature and hazard mapping

Daily maximum and minimum air temperatures ( $T_{max}$  and  $T_{min}$ ) were modeled using a stacking ensemble machine learning algorithm (see [method details](#)). Data from a total of 107 weather stations in Seoul (Figure 1A) were used as *in situ* air temperatures for the modeling. Figures 2A and 2D show the leave-one-station-out cross-validation prediction performance for  $T_{max}$  and  $T_{min}$ , respectively. Our proposed stacking ensemble algorithm demonstrates very high validation accuracy ( $R^2 = 0.958$  and root-mean-square error (RMSE)  $\sim 0.62^\circ\text{C}$  for  $T_{max}$ ,  $R^2 = 0.933$  and RMSE  $\sim 0.77^\circ\text{C}$  for  $T_{min}$ ).

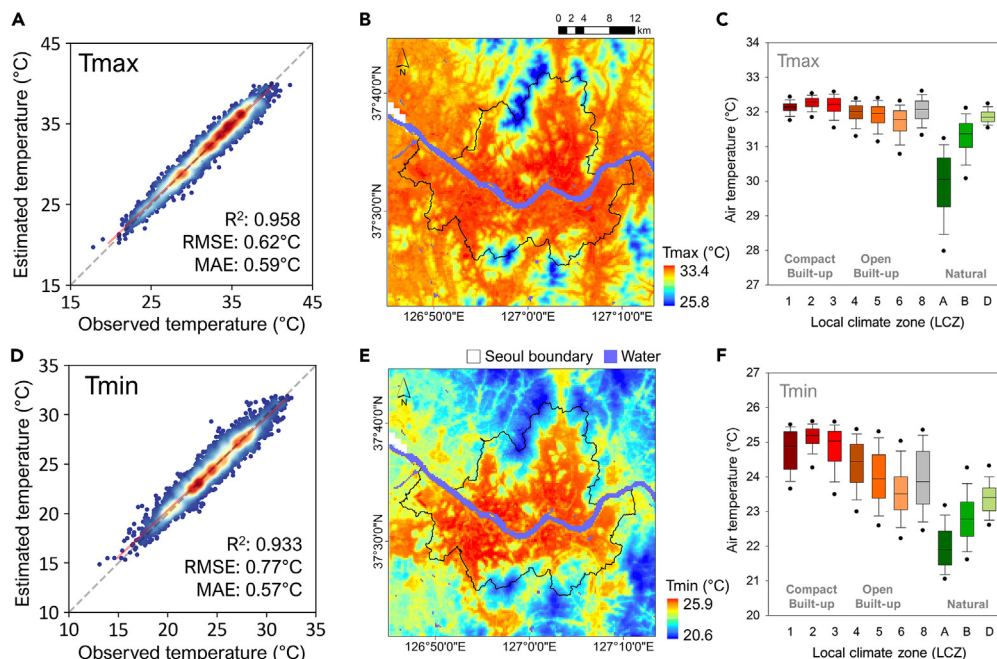


**Figure 2. Estimated air temperatures and their spatial distributions**

(A) Density scatterplots of the estimated and observed maximum air temperatures for the leave-one-station-out cross-validation (LOSOCV) results for Tmax. See also Figure S2.

(B) Spatial distribution of average Tmax.

(C) Boxplots of the average Tmax patterns for each LCZ class.

(D) Density scatterplots of the estimated and observed minimum air temperatures for the leave-one-station-out cross-validation (LOSOCV) results for Tmin. See also Figure S3.

(E) Spatial distribution of average Tmin.

(F) Boxplots of the average Tmin patterns for each LCZ class. The color scheme in the scatterplots, which transitions from blue to red, represents the increasing density of the paired samples.

Based on the developed model, we produced maps of the average Tmax and Tmin for the summer of 2018 and examined the temperature distribution according to the Local Climate Zone (LCZ) classification (Figures 2B and 2C and 2E–2F). The LCZ is suitable for characterizing urban thermal climate.<sup>25</sup> Seoul has eleven LCZ classes (Figure 1B): seven urban-type LCZs (three compact-type, LCZ1–3), three open-type (LCZ4–6 and LCZ 8), and four natural-type LCZs (LCZA–B, D, and G). Tmax and Tmin exhibited divergent spatial distributions in Seoul. During the daytime, most surface types, except for densely vegetated areas (i.e., LCZ A), experienced significant warming owing to the predominant influence of incoming solar radiation.<sup>26</sup> In contrast, the nighttime conditions displayed rapid cooling of vegetated regions, while the urban areas maintained elevated temperatures for extended periods, which was attributable to the re-emission of the heat absorbed by impervious surfaces.<sup>27</sup> Consequently, Tmin demonstrated pronounced temperature gradients between urban and vegetated surfaces, a phenomenon commonly referred to as the urban heat island effect. Furthermore, the compact-type LCZs (LCZ1–3) generally exhibited higher Tmin values than the other LCZ classes, followed by the open type (LCZ 4–6) and natural types (LCZ A, B, and D; refer to the boxplots in Figures 2C and 2F). Notably, regions with tall buildings were associated with increased Tmin values, particularly in the open-type LCZs.

Figures 3A and 3B present the average daily daytime and nighttime hazards, respectively, derived from the cumulative two-day estimations of Tmax and Tmin. During the day, regions with relatively high hazards were more concentrated in the eastern portion of the city than at night. These disparities could be attributed to an array of meteorological and urban structural factors. For example, the prevailing seasonal westerly winds in summer contribute to the cooling of the western side of the city during the daytime.<sup>29</sup> Furthermore, areas characterized by a substantial proportion of open-type LCZs, situated on the periphery of the city, exhibited comparatively lower hazards, particularly at night.

The daily hazard devised in this study exhibited noticeable temporal variations, primarily owing to the use of daily air temperatures as indicators (Figure 3C; August 2018). For instance, during the early days of August (August 2–3), which marked the hottest days of 2018, the hazard was distinctly high and subsequently diminished toward the end of August (August 27–28; see the red bold line in Figure 3C). The spatial distribution of daily hazards across the 424 *dongs* also demonstrated temporal variations (refer to the range of the boxplots in Figure 3C). Generally, daytime hazards exhibit a narrower range than nighttime hazards.

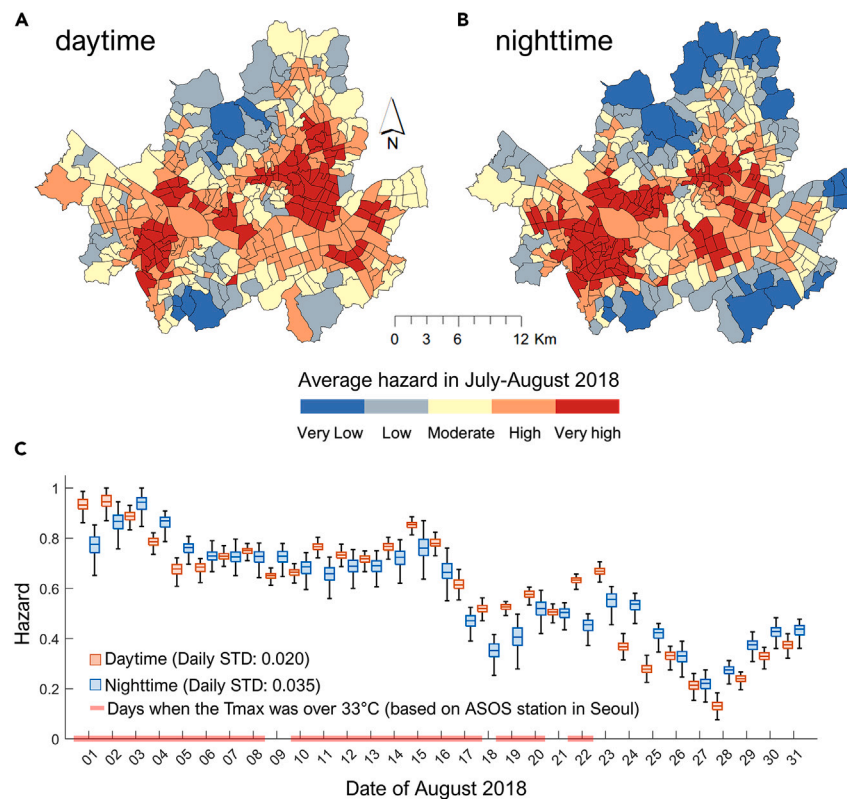


**Figure 3. Hazard distribution**

(A) Map of average daytime hazards, July–August, 2018. Each hazard map was clustered into five grades based on the Jenks natural breaks classification.

(B) Map of average nighttime hazards, July–August 2018. See also [Figure S1](#).

(C) Temporal distribution of boxplots for daily hazards in 424 administrative *dong* for daytime (red) and nighttime (blue), August 2018. The daily STD represents the August average standard deviation of the daily hazard for 424 *dong*. The red bold lines in [Figure 3C](#) indicate the days with Tmax exceeding 33°C, observed from the automated surface observing systems (ASOS) in Seoul.

### Exposure and vulnerability maps

[Figures 4A](#) and [4B](#) display the average exposure using the *de facto* population data for daytime (3:00 p.m.) and nighttime (6:00 a.m.), respectively. Notably, there was a pronounced difference in the distribution of daytime and nighttime exposure when considering the *de facto* population. During the day, regions with a high density of workplaces, such as Jongro 1–4 *dong* and Myeong-*dong* in Jongno and Jung-gu (referred to as A) and Nonhyeon and Yeoksam-*dong* in Gangnam-gu (referred to as B), exhibited elevated *de facto* exposure. Conversely, high exposure regions emerged in the eastern and southwestern parts of Seoul at night. These areas possess a relatively high proportion of housing as people return home at night. It is worth noting that *de jure* exposure ([Figure 4C](#)) demonstrated a spatial distribution more similar to that of *de facto* nighttime than daytime exposure.

[Figure 4D](#) depicts the daily spatial correlation between the *de facto* and *de jure* populations during the day and night. The weekend and weekday correlations displayed significant differences during the daytime. This may be attributed to people being relatively more active near their residential areas on weekends. Conversely, there was virtually no correlation during the daytime on weekdays, indicating that the floating population in a megacity such as Seoul exhibits a markedly different distribution from that of the census population. Both weekdays and weekends exhibited a substantial correlation at night, with the correlation being marginally more pronounced during the weekends.

[Figure 5](#) presents the average heat vulnerability for the daytime and nighttime. There were no discernible spatial differences in the vulnerability maps between daytime and nighttime, in contrast to those of hazard and exposure. Vulnerability displayed a stronger positive-skewness distribution during both the daytime and nighttime than hazard and exposure (see [Figure S1](#)). Specifically, high vulnerability areas were concentrated in the northeastern part of the city during both the day and night. Region A exhibited very high vulnerability and exposure ([Figures 4A](#) and [5A](#)) during the day. In contrast, Region B displayed the opposite pattern: high daytime exposure ([Figure 4A](#)) but very low vulnerability ([Figure 5A](#)). Region B, a part of Gangnam-gu, had a high percentage of relatively young people (both *de jure* and *de facto*, not shown) who are less vulnerable to heat.

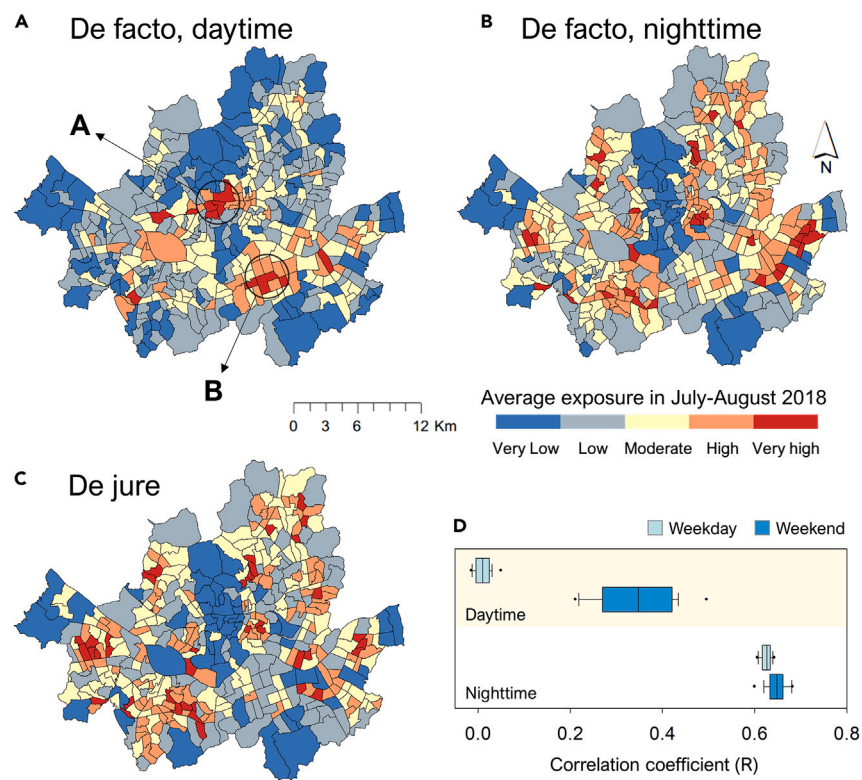


**Figure 4. Exposure distribution**

(A) Map of average daytime exposure using *de facto* population, July–August 2018. Each exposure map was clustered into five grades based on the Jenks natural breaks classification.

(B) Map of average nighttime exposure using *de facto* population, July–August 2018. See also [Figure S1](#).

(C) Map of average exposure using *de jure* population, July–August 2018.

(D) Boxplots of the correlation between *de facto* and *de jure* exposure on weekdays and weekends for daytime and nighttime.

### Heat risk mapping and validation

Finally, we produced daily daytime and nighttime heat risk estimates by combining the three component layers: hazard, exposure, and vulnerability ([Figure 6](#)). The spatial distribution of the risk during the day and night exhibited noticeable disparities. This can be attributed to the distinct distributions of hazards and exposure during the daytime and nighttime, which are the two components that constitute risk. During the daytime, high-risk and very-high-risk areas were predominantly concentrated in the central-northern region of the city. Notably, areas such as Jongro 1–4, Euljiro, and Hoehyeon-*dong* demonstrated a significantly elevated daytime risk. In this region, high and very high hazard levels emerged during the daytime ([Figure 3A](#)), and it was evident that exposure and vulnerability were also densely concentrated ([Figures 4A and 5A](#)). In contrast to those during the daytime, high-risk regions at night were dispersed across the city, including areas such as Gayang 2, Bugahyeon, and Cheongho 3-*dong*.

[Figure 7](#) presents the validation results for the spatially normalized heat risk using the average heat-related illness ratio from 2018. The daytime heat risk map generated by the proposed framework demonstrated a significantly high correlation ( $R = 0.8$ ) with the heat-related illness ratio. In contrast, the nighttime heat risk exhibited a relatively low correlation. This finding suggests that the spatial distribution of heat-related illness occurrence is more closely associated with risk during the day than at night. We also compared our proposed heat risk framework with a conventional approach that uses only the *de jure* population to calculate exposure and vulnerability (see [STAR Methods](#)). Our proposed heat risk model displayed superior correlation performance to the risk maps created using only the *de jure* population ( $R = 0.09$  for daytime and  $R = 0.07$  for nighttime).

[Table 1](#) is a contingency table outlining the relationship between the daily number of heat-related illnesses and daily heat risk for the three representative gu regions in Seoul. Daytime heat risk demonstrated promising performance across all three regions (probability of detection (POD): 0.96–1, false alarm rate (FAR) < 0.39, critical success index (CSI): 0.61–0.68). Although the performance of nighttime heat risk was lower than that of daytime, regions such as Dobong-gu—where the highest number of heat-related illnesses occurred in 2018—displayed a relatively strong temporal association with heat-related illnesses, even during the nighttime (POD: 0.95, FAR: 0.34, CSI: 0.64).

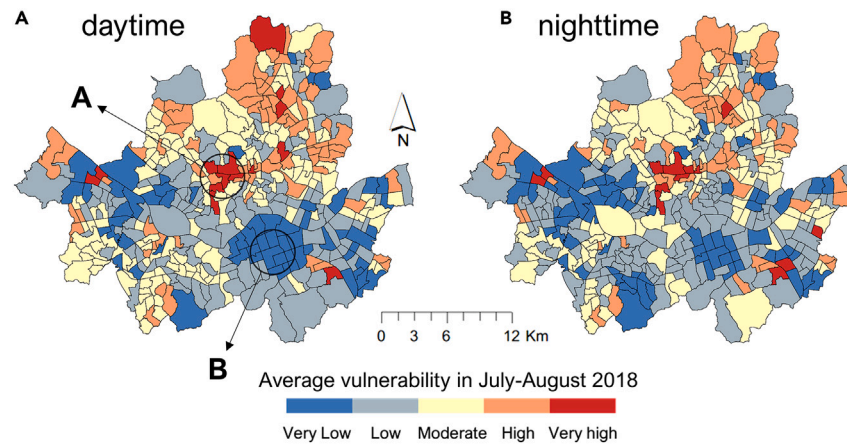


**Figure 5. Vulnerability distribution**

(A) Map of average daytime vulnerabilities, July–August 2018. Each vulnerability map was clustered into five grades based on the Jenks natural breaks classification.

(B) Map of average nighttime vulnerabilities, July–August 2018. See also [Figure S1](#).

## DISCUSSION

### The superiority of air temperature-based heat hazard maps

This study produced high-resolution (250 m) daily Tmax and Tmin values using machine learning techniques. The stacking ensemble machine learning method employed showed superior performance to conventional air temperature interpolation methods, such as cokriging and other single models (i.e., multi-linear regression, support vector regression, and local linear forest; see [Figures S2](#) and [S3](#)). In particular, the stacking-based approach exhibited a significantly improved ability to model the spatial distribution of temperatures compared to the other single models for both Tmax and Tmin ([Table 2](#)). This implies that our air temperature maps can accurately reflect spatial variations in heat hazards and help monitor temperature differences between daytime and nighttime.

Heat hazard maps derived from these air temperatures offer several advantages over those derived in previous studies.<sup>9,11,15,19,30</sup> By using air temperature instead of LST as the source of heat hazard, our maps corresponded better to the population’s actual heat exposure. Moreover, previous studies often used LST from a single date<sup>30</sup> or long-term average LST,<sup>11</sup> making it difficult to capture the temporal variability of heat hazards. For example, only four Landsat images were acquired during the study period (12 July 2018, 13 August 2018, 28 July 2018, and 29 August 2018). However, these images are predominantly obscured by cloud cover. In particular, the two images exhibiting relatively lower cloud rates, captured on July 28 and August 13, 2018, failed to provide a seamless representation of LST (cloud cover rates of 23% and 47%, respectively). Consequently, applying these LST images to analyze the spatial distribution of heat hazards proved challenging.

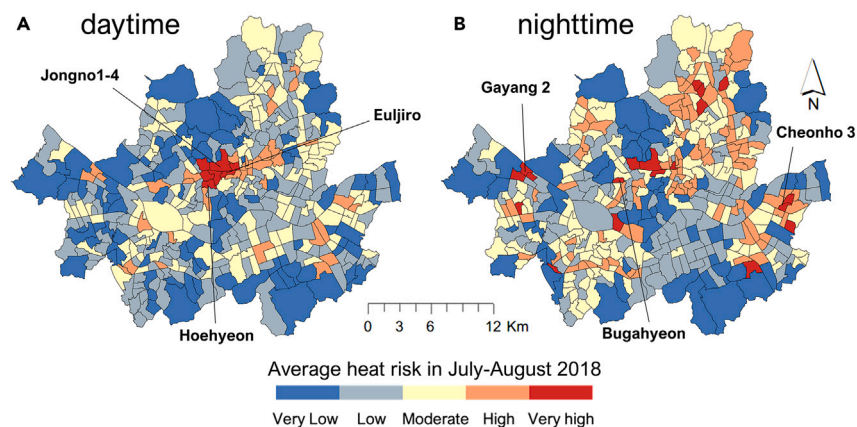


**Figure 6. Heat risk distribution**

(A) Map of average daytime heat risk, July–August 2018. Each heat risk map was clustered into five grades based on the Jenks natural breaks classification.

(B) Map of average nighttime heat risk, July–August 2018. See also [Figure S1](#). Three representative *dongs* with the largest heat risks during the daytime and nighttime are presented in (A) and (B), respectively.

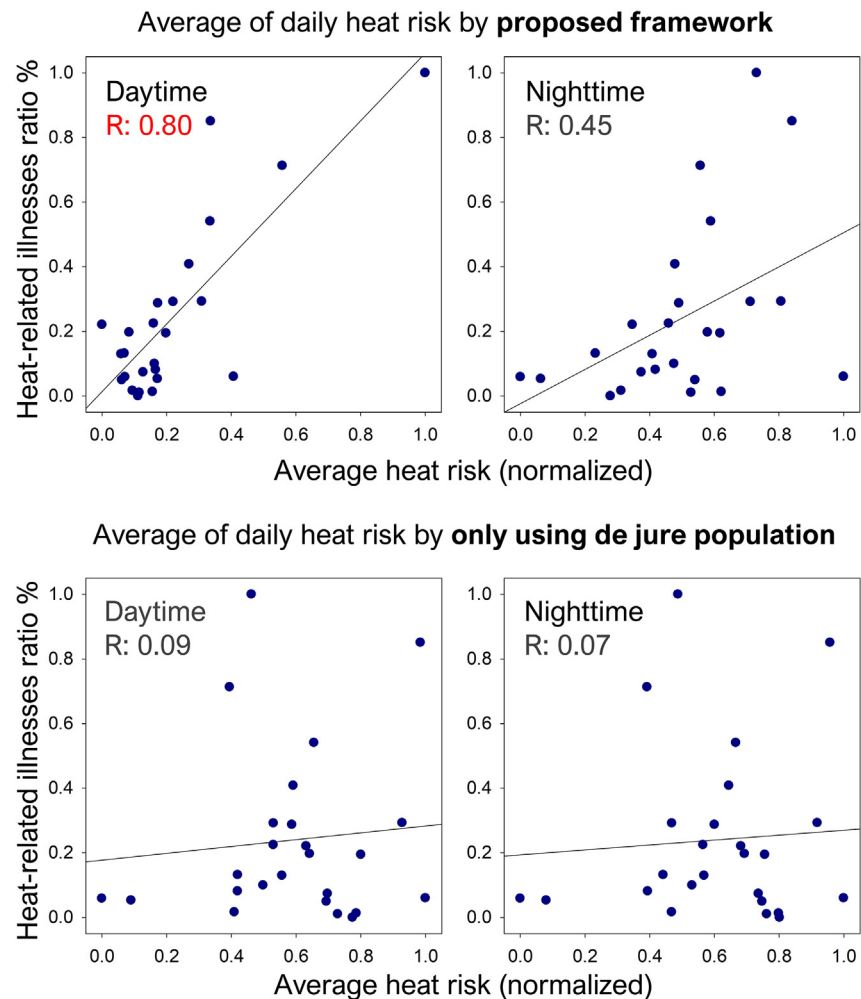


**Figure 7. Validation of the heat risk map, using the heat-related illness ratios**

Scatterplots of spatially normalized average heat risk for July–August 2018 and heat-related illness ratio (%) for 25 *gu* in Seoul during the daytime and nighttime. The heat risks calculated with the proposed framework (top) and using only the *de jure* population (bottom) are compared.

Furthermore, prior research employing LST data as a heat exposure source encountered limitations in depicting the maximum heat exposure duration (e.g., 2–3 p.m., the time when maximum air temperatures usually occur) owing to fixed satellite-acquisition times, such as Landsat LST captured at 10:30 a.m.

Our daily air temperature maps effectively showed the day-to-day variation in daytime and nighttime heat hazards, where high hazards appeared more prominent on extreme heat days. Using the LCZ and produced air temperatures, we demonstrated that our hypothesis is valid when the spatial distribution of air temperature varies with the urban structure, and these differences are present both during the day and at night. We confirmed that these phenomena produced a spatiotemporally heterogeneous heat hazard map. Overall, the use of air temperature data at high spatiotemporal resolution provides a more relevant assessment of heat hazards to human health.

### The effectiveness of *de facto* population-based heat risk maps

In this study, we measured a diurnal heat exposure using *de facto* population data. Many previous studies have calculated heat exposure using *de jure* population data;<sup>9,15,19,30,31</sup> however, according to our findings, *de jure* population does not accurately reflect the actual population distribution in the daytime when many people are away from home. Furthermore, our heat risk map enabled the simulation of heat risk changes based on population fluctuations between weekdays and weekends. We found that the floating (*de facto*) population during the day in a megacity such as Seoul has a very different distribution from the census (*de jure*) population, particularly on weekdays.

**Table 1. Contingency table for the daily heat risk (daytime and nighttime) and number of heat-related illnesses**

	POD	FAR	CSI
<b>Daytime heat risk</b>			
Dobong-gu (90)	1.00	0.39	0.61
Dongdaemun-gu (61)	0.96	0.30	0.68
Yeongdeungpo-gu (51)	0.96	0.34	0.64
<b>Nighttime heat risk</b>			
Dobong-gu (90)	0.95	0.34	0.64
Dongdaemun-gu (61)	0.74	0.38	0.51
Yeongdeungpo-gu (51)	0.71	0.45	0.45

Assessment of the three representative *gu* regions with the largest number of illnesses during July–August 2018. Numbers in parentheses indicate the number of heat-related illnesses. The thresholds were set to the average value of the daily heat risk and a daily number of heat-related illnesses for each *gu*.

When the diurnal heat risk map developed in this study was validated using heat-related illness data, it exhibited a higher spatial correlation during the day than at night. The daytime heat risk map incorporated  $T_{max}$ , which typically occurs at approximately 2–3 p.m. in Seoul, and daytime *de facto* population data. This finding aligns with the Korea Centers for Disease Control and Prevention report,<sup>32</sup> which indicates that heat-related illnesses in Seoul frequently occur between 2 p.m. and 3 p.m. (daytime). The daytime heat risk map proposed by our framework effectively represents the daily temporal patterns of heat-related illness cases (Table 2).

Compared to previous heat risk studies that produced maps on a yearly scale,<sup>10,11,18,19</sup> our proposed framework can generate risk maps on a daily scale. The validation results shown in Figure 7 and Table 1 suggest that our heat risk maps, especially for daytime, effectively provide both spatial and temporal trends of heat-related illness occurrences in Seoul. While many heat risk or vulnerability mapping studies have not been validated owing to a lack of reference data,<sup>10,15,18,19,30,31</sup> our study established the reliability of the proposed framework by directly validating the risk using heat-related illness data.

## LIMITATIONS OF THE STUDY

Owing to data acquisition challenges, we used certain factors (i.e., elderly men and women living alone, persons with disabilities, and recipients of basic livelihoods) for vulnerability mapping based on *de jure* populations. Acquiring these data based on the *de facto* population would enable a more realistic heat risk mapping. Future studies should incorporate additional variables related to socioeconomic vulnerability.

The heat-related illness data used for validation also have limitations. Although the data were obtained from all designated emergency rooms of hospitals in Seoul, they may not cover all heat-related illnesses in the city, as some patients may have reported to other medical institutions or not at all. Furthermore, the currently available heat-related illness data have a spatial scale (i.e., *gu* level) relatively coarse for the purpose of validating our calculated heat risk at the *dong* level. This study also merged hazard, exposure, and vulnerability for risk mapping without a universal rule, leaving the optimization of weights for combining the three components for further investigation.

This case study was conducted in Seoul, South Korea, in 2018. If data are available (e.g., dense weather stations and *de facto* population) for other cities, it is recommended that the proposed framework be evaluated in multiple cities to ensure robust generalization. Future studies could develop tailored, dynamic risk-governance strategies based on the suggested diurnal heat risk mapping framework in different urban environments. In addition, the exploration of scenario-based heat risk projections in future research is promising. Once future predictions of *de facto* population become attainable, researchers can integrate shared socioeconomic pathway scenario-based vulnerability with

**Table 2. Average of the daily spatial correlation results**

$T_{max}$	Cokriging	MLR	SVR	LLF	Stacking
R	0.411	0.645	0.650	0.657	<b>0.703</b>
RMSE (°C)	1.001	0.840	0.834	0.821	<b>0.785</b>
MAE (°C)	0.743	0.645	0.640	0.630	<b>0.594</b>
$T_{min}$	Cokriging	MLR	SVR	LLF	Stacking
R	0.584	0.741	0.759	0.761	<b>0.782</b>
RMSE (°C)	0.965	0.794	0.770	0.764	<b>0.747</b>
MAE (°C)	0.767	0.608	0.588	0.581	<b>0.565</b>

The correlation coefficient (R), root-mean-square error (RMSE), and mean absolute error (MAE) from leave-one-station-out cross-validation (LOSOCV) results based on five spatial models of daily  $T_{max}$  and  $T_{min}$  during the study period. The best results are highlighted in bold.

representative concentration pathway climate model-based heat hazard projections to provide more comprehensive insights into potential heat risks.<sup>33,34</sup>

## STAR★METHODS

Detailed methods are provided in the online version of this paper and include the following:

- KEY RESOURCES TABLE
- RESOURCE AVAILABILITY
  - Lead contact
  - Materials availability
  - Data and code availability
- METHOD DETAILS
  - Study area and data collection
  - Heat risk mapping framework

## SUPPLEMENTAL INFORMATION

Supplemental information can be found online at <https://doi.org/10.1016/j.isci.2023.108123>.

## ACKNOWLEDGMENTS

This research is supported by Korea Environment Industry & Technology Institute (KEITI) through Digital Infrastructure Building Project for Monitoring, Surveying, and Evaluating the Environmental Health, funded by Korea Ministry of Environment (MOE) (2021003330001 (NTIS: 1485017948)), the Korea Meteorological Administration Research and Development Program under Grant KMIPA 2017–2010, and the National Research Foundation of Korea (NRF) (NRF-2021R1A2C2008561).

## AUTHOR CONTRIBUTIONS

C.Y.: conceptualization, methodology, analysis, writing – original draft, writing – review & editing; J.I.: conceptualization, methodology, writing – review & editing, supervision; Q.W.: writing – review & editing, supervision; D.C.: methodology, writing – review & editing; E.K.: writing – review & editing; Y.S.: Writing – review & editing.

## DECLARATION OF INTERESTS

The authors declare no competing interests.

Received: June 14, 2023

Revised: September 5, 2023

Accepted: September 29, 2023

Published: October 4, 2023

## REFERENCES

1. Schär, C. (2016). The worst heat waves to come. *Nat. Clim. Chang.* 6, 128–129.
2. Perkins, S.E., Alexander, L.V., and Nairn, J.R. (2012). Increasing frequency, intensity and duration of observed global heatwaves and warm spells. *Geophys. Res. Lett.* 39.
3. Peng, R.D., Bobb, J.F., Tebaldi, C., McDaniel, L., Bell, M.L., and Dominici, F. (2011). Toward a quantitative estimate of future heat wave mortality under global climate change. *Environ. Health Perspect.* 119, 701–706.
4. Anderson, G.B., and Bell, M.L. (2011). Heat waves in the United States: mortality risk during heat waves and effect modification by heat wave characteristics in 43 US communities. *Environ. Health Perspect.* 119, 210–218.
5. McKechnie, A.E., and Wolf, B.O. (2010). Climate change increases the likelihood of catastrophic avian mortality events during extreme heat waves. *Biol. Lett.* 6, 253–256.
6. Son, J.-Y., Lee, J.-T., Anderson, G.B., and Bell, M.L. (2012). The impact of heat waves on mortality in seven major cities in Korea. *Environ. Health Perspect.* 120, 566–571.
7. Satterthwaite, D., Archer, D., Colenbrander, S., Dodman, D., Hardoy, J., Mitlin, D., and Patel, S. (2020). Building resilience to climate change in informal settlements. *One Earth* 2, 143–156.
8. Crichton, D. (1999). The risk triangle. *Natural disaster management* 102, 102–103.
9. Estoque, R.C., Ooba, M., Seposo, X.T., Togawa, T., Hijjoka, Y., Takahashi, K., and Nakamura, S. (2020). Heat health risk assessment in Philippine cities using remotely sensed data and social-ecological indicators. *Nat. Commun.* 11, 1581.
10. Hua, J., Zhang, X., Ren, C., Shi, Y., and Lee, T.-C. (2021). Spatiotemporal assessment of extreme heat risk for high-density cities: A case study of Hong Kong from 2006 to 2016. *Sustain. Cities Soc.* 64, 102507.
11. Song, J., Huang, B., Kim, J.S., Wen, J., and Li, R. (2020). Fine-scale mapping of an evidence-based heat health risk index for high-density cities: Hong Kong as a case study. *Sci. Total Environ.* 718, 137226.
12. Hutengs, C., and Vohland, M. (2016). Downscaling land surface temperatures at regional scales with random forest regression. *Remote Sensing of Environment* 178, 127–141.
13. Ho, H.C., Knudby, A., Sirovyak, P., Xu, Y., Hodul, M., and Henderson, S.B. (2014). Mapping maximum urban air temperature on hot summer days. *Remote Sensing of Environment* 154, 38–45.
14. Cho, D., Yoo, C., Im, J., Lee, Y., and Lee, J. (2020). Improvement of spatial interpolation accuracy of daily maximum air temperature in urban areas using a stacking ensemble technique. *GIScience Remote Sens.* 57, 633–649.
15. Morabito, M., Crisci, A., Gioli, B., Gualtieri, G., Toscano, P., Di Stefano, V., Orlandini, S., and Gensini, G.F. (2015). Urban-hazard risk analysis: Mapping of heat-related risks in the

- elderly in major Italian cities. *PLoS One* 10, e0127277.
16. Tomlinson, C.J., Chapman, L., Thornes, J.E., and Baker, C.J. (2011). Including the urban heat island in spatial heat health risk assessment strategies: a case study for Birmingham, UK. *Int. J. Health Geogr.* 10, 42.
  17. Verdonck, M.-L., Demuzere, M., Hooyberghs, H., Priem, F., and Van Coillie, F. (2019). Heat risk assessment for the Brussels capital region under different urban planning and greenhouse gas emission scenarios. *J. Environ. Manage.* 249, 109210.
  18. Holec, J., Šveda, M., Szatmári, D., Feranec, J., Bobálová, H., Kopecká, M., and Štastný, P. (2021). Heat risk assessment based on mobile phone data: case study of Bratislava, Slovakia. *Nat. Hazards* 108, 3099–3120.
  19. Navarro-Estupiñan, J., Robles-Morua, A., Díaz-Caravantes, R., and Vivoni, E.R. (2020). Heat risk mapping through spatial analysis of remotely-sensed data and socioeconomic vulnerability in Hermosillo, México. *Urban Clim.* 31, 100576.
  20. Beckx, C., Int Panis, L., Arentz, T., Janssens, D., Torfs, R., Broekx, S., and Wets, G. (2009). A dynamic activity-based population modelling approach to evaluate exposure to air pollution: Methods and application to a Dutch urban area. *Environ. Impact Assess. Rev.* 29, 179–185.
  21. Tsin, P.K., Knudby, A., Krayenhoff, E.S., Ho, H.C., Brauer, M., and Henderson, S.B. (2016). Microscale mobile monitoring of urban air temperature. *Urban Clim.* 18, 58–72.
  22. Arellano, B., and Roca, J. (2021). Remote sensing and night time urban heat island. *Int. Arch. Photogramm. Remote Sens. Spatial Inf. Sci.* 43, 15–22.
  23. Zhou, D., Zhao, S., Liu, S., Zhang, L., and Zhu, C. (2014). Surface urban heat island in China's 32 major cities: Spatial patterns and drivers. *Remote Sensing of Environment* 152, 51–61.
  24. Zhang, C., Li, M., Ma, D., and Guo, R. (2021). How Different Are Population Movements between Weekdays and Weekends: A Complex-Network-Based Analysis on 36 Major Chinese Cities. *Land* 10, 1160.
  25. Stewart, I.D., and Oke, T.R. (2012). Local climate zones for urban temperature studies. *Bull. Am. Meteorol. Soc.* 93, 1879–1900.
  26. Oke, T.R., Mills, G., Christen, A., and Voogt, J.A. (2017). *Urban Climates* (Cambridge University Press).
  27. Li, D., Bou-Zeid, E., and Oppenheimer, M. (2014). The effectiveness of cool and green roofs as urban heat island mitigation strategies. *Environ. Res. Lett.* 9, 055002.
  28. Yoo, C., Lee, Y., Cho, D., Im, J., and Han, D. (2020). Improving local climate zone classification using incomplete building data and Sentinel 2 images based on convolutional neural networks. *Rem. Sens.* 12, 3552.
  29. Pokhrel, R., and Lee, H. (2011). Estimation of the effective zone of sea/land breeze in a coastal area. *Atmos. Pollut. Res.* 2, 106–115.
  30. Sun, Y., Li, Y., Ma, R., Gao, C., and Wu, Y. (2022). Mapping urban socio-economic vulnerability related to heat risk: A grid-based assessment framework by combining the geospatial big data. *Urban Clim.* 43, 101169.
  31. Dong, J., Peng, J., He, X., Corcoran, J., Qiu, S., and Wang, X. (2020). Heatwave-induced human health risk assessment in megacities based on heat stress-social vulnerability-human exposure framework. *Landscape Urban Plann.* 203, 103907.
  32. KCDC Annual report on the notified patients with heat-related illness in Korea (in Korean). Korea Centers for Disease Control and Prevention.
  33. Zhuang, H., Chen, G., Yan, Y., Li, B., Zeng, L., Ou, J., Liu, K., and Liu, X. (2022). Simulation of urban land expansion in China at 30 m resolution through 2050 under shared socioeconomic pathways. *GIScience Remote Sens.* 59, 1301–1320.
  34. Chen, G., Zhuang, H., and Liu, X. (2023). Cell-level coupling of a mechanistic model to cellular automata for improving land simulation. *GIScience Remote Sens.* 60, 2166443.
  35. Yang, H.J. (2021). Visualizing spatial disparities in population aging in the Seoul Metropolitan Area. *Environ. Plan. A.* 53, 879–882.
  36. Ermida, S.L., Soares, P., Mantas, V., Götttsche, F.M., and Trigo, I.F. (2020). Google earth engine open-source code for land surface temperature estimation from the landsat series. *Rem. Sens.* 12, 1471.
  37. Yoo, C., Im, J., Cho, D., Lee, Y., Bae, D., and Sismanidis, P. (2022). Downscaling MODIS nighttime land surface temperatures in urban areas using ASTER thermal data through local linear forest. *Int. J. Appl. Earth Obs. Geoinf.* 110, 102827.
  38. Chen, C., Bagan, H., and Yoshida, T. (2023). Multiscale mapping of local climate zones in Tokyo using airborne LiDAR data, GIS vectors, and Sentinel-2 imagery. *GIScience Remote Sens.* 60, 2209970.
  39. Kang, C.-D. (2020). Effects of the human and built environment on neighborhood vitality: Evidence from Seoul, Korea, using mobile phone data. *J. Urban Plan. Dev.* 146, 05020024.
  40. Park, C.-E., Jeong, S., Harrington, L.J., Lee, M.-I., and Zheng, C. (2020). Population ageing determines changes in heat vulnerability to future warming. *Environ. Res. Lett.* 15, 114043.
  41. Venter, Z.S., Brousse, O., Esau, I., and Meier, F. (2020). Hyperlocal mapping of urban air temperature using remote sensing and crowdsourced weather data. *Remote Sensing of Environment* 242, 111791.
  42. Nichol, J.E., and Wong, M.S. (2008). Spatial variability of air temperature and appropriate resolution for satellite-derived air temperature estimation. *Int. J. Rem. Sens.* 29, 7213–7223.
  43. Zhou, T., and Jiao, H. (2023). Exploration of the stacking ensemble machine learning algorithm for cheating detection in large-scale assessment. *Educ. Psychol. Meas.* 83, 831–854.
  44. Hines, B., Qian, G., and Tordesillas, A. (2022). Mapping Australia's precipitation: harnessing the synergies of multi-satellite remote sensing and gauge network data. *GIScience Remote Sens.* 59, 2084–2110.
  45. Jang, E., Kim, Y.J., Im, J., and Park, Y.G. (2021). Improvement of SMAP sea surface salinity in river-dominated oceans using machine learning approaches. *GIScience Remote Sens.* 58, 138–160.
  46. Zhang, Y., Ma, J., Liang, S., Li, X., and Liu, J. (2022). A stacking ensemble algorithm for improving the biases of forest aboveground biomass estimations from multiple remotely sensed datasets. *GIScience Remote Sens.* 59, 234–249.
  47. Bobb, J.F., Obermeyer, Z., Wang, Y., and Dominici, F. (2014). Cause-specific risk of hospital admission related to extreme heat in older adults. *JAMA* 312, 2659–2667.
  48. Bao, J., Li, X., and Yu, C. (2015). The construction and validation of the heat vulnerability index, a review. *Int. J. Environ. Res. Public Health* 12, 7220–7234.
  49. Bessah, E., Raji, A.O., Taiwo, O.J., Agodzo, S.K., Oloade, O.O., Strapasson, A., and Donkor, E. (2021). Gender-based variations in the perception of climate change impact, vulnerability and adaptation strategies in the Pra River Basin of Ghana. *Int. J. Clim. Chang. Strateg. Manag.* 13, 435–462.
  50. Green, H., Bailey, J., Schwarz, L., Vanos, J., Ebi, K., and Benmarhnia, T. (2019). Impact of heat on mortality and morbidity in low and middle income countries: a review of the epidemiological evidence and considerations for future research. *Environ. Res.* 171, 80–91.
  51. Niu, Y., Li, Z., Gao, Y., Liu, X., Xu, L., Vardoulakis, S., Yue, Y., Wang, J., and Liu, Q. (2021). A systematic review of the development and validation of the heat vulnerability index: major factors, methods, and spatial units. *Curr. Clim. Change Rep.* 7, 87–97.
  52. Wolf, T., and McGregor, G. (2013). The development of a heat wave vulnerability index for London, United Kingdom. *Weather Clim. Extrem.* 1, 59–68.
  53. Hoehne, C.G., Hondula, D.M., Chester, M.V., Eisenman, D.P., Middel, A., Fraser, A.M., Watkins, L., and Gerster, K. (2018). Heat exposure during outdoor activities in the US varies significantly by city, demography, and activity. *Health Place* 54, 1–10.
  54. Nayak, S.G., Shrestha, S., Kinney, P.L., Ross, Z., Sheridan, S.C., Pantea, C.I., Hsu, W.H., Muscatello, N., and Hwang, S.-A. (2018). Development of a heat vulnerability index for New York State. *Publ. Health* 161, 127–137.
  55. Bhatt, P., and Maclean, A.L. (2023). Comparison of high-resolution NAIP and unmanned aerial vehicle (UAV) imagery for natural vegetation communities classification using machine learning approaches. *GIScience Remote Sens.* 60, 2177448.
  56. Kaiser, H.F. (1960). The application of electronic computers to factor analysis. *Educ. Psychol. Meas.* 20, 141–151.
  57. Schmidlein, M.C., Deutsch, R.C., Piegorsch, W.W., and Cutter, S.L. (2008). A sensitivity analysis of the social vulnerability index. *Risk Anal.* 28, 1099–1114.
  58. Zhang, W., Zheng, C., and Chen, F. (2019). Mapping heat-related health risks of elderly citizens in mountainous area: A case study of Chongqing, China. *Sci. Total Environ.* 663, 852–866.
  59. Wolf, T., McGregor, G., and Analitis, A. (2014). Performance assessment of a heat wave vulnerability index for greater London, United Kingdom. *Weather, climate, and society* 6, 32–46.

## STAR★METHODS

## KEY RESOURCES TABLE

REAGENT or RESOURCE	SOURCE	IDENTIFIER
<i>Deposited data</i>		
<i>In situ</i> air temperatures from automatic weather stations	Korea Meteorological Administration (KMA)	<a href="https://data.kma.go.kr">https://data.kma.go.kr</a>
<i>In situ</i> air temperatures two from forest meteorological stations	National Institute of Forest Science, South Korea	<a href="http://mw.nifos.go.kr">http://mw.nifos.go.kr</a>
Digital elevation model (DEM)	USGS	<a href="https://earthexplorer.usgs.gov">https://earthexplorer.usgs.gov</a>
Road data	Open Street Map	<a href="http://www.openstreetmap.org">www.openstreetmap.org</a>
Global Human Settlement population and built-up surface	European Commission	<a href="https://ghsl.jrc.ec.europa.eu/download.php">https://ghsl.jrc.ec.europa.eu/download.php</a>
Wind speed	Global Wind Atlas	<a href="https://globalwindatlas.info">https://globalwindatlas.info</a>
Landsat 8 satellite image	USGS	<a href="https://earthexplorer.usgs.gov">https://earthexplorer.usgs.gov</a>
<i>De facto</i> population	Public data portal, Korea	<a href="https://www.data.go.kr/">https://www.data.go.kr/</a>
<i>De jure</i> population	Seoul Statistical Information System	<a href="https://data.seoul.go.kr/">https://data.seoul.go.kr/</a>
<i>In situ</i> air temperatures from automatic weather stations	Korea Meteorological Administration (KMA)	<a href="https://data.kma.go.kr">https://data.kma.go.kr</a>
<i>Software and algorithm</i>		
MATLAB	Mathworks	<a href="https://www.mathworks.com/products/matlab.html">https://www.mathworks.com/products/matlab.html</a>
Google Earth Engine	Google	<a href="https://earthengine.google.com/">https://earthengine.google.com/</a>
ArcGIS	ESRI	<a href="https://www.esri.com/">https://www.esri.com/</a>

## RESOURCE AVAILABILITY

## Lead contact

All requests for additional information and resources should be directed to the lead contact, Jungho Im ([ersgis@unist.ac.kr](mailto:ersgis@unist.ac.kr))

## Materials availability

This study did not generate new unique reagents.

## Data and code availability

All data can be obtained from the lead contact, provided the request is reasonable.

The code related to the developed model can be accessed by reaching out to the [lead contact](#).

## METHOD DETAILS

## Study area and data collection

*Study area*

Seoul, which is situated in the midwestern region of the Korean Peninsula, is a highly urbanized city with a diverse distribution of building types (Figure 1). The city extends approximately 60 km inland from the western coast and is bisected by the Han River, with the northern and southern regions further demarcated by four mountains. Administratively, Seoul is divided into 424 *dong* districts, which are the smallest administrative units, and 25 *gu* districts, intermediary units between the *dong* and city levels. Categorized as having a humid subtropical climate under the Köppen-Geiger climate classification system, Seoul experiences hot and humid summers influenced by the East Asian monsoon. Seoul is a densely populated metropolitan area with a population of approximately 9.5 million residents occupying an area of 605.2 km<sup>2</sup>. Despite an overall declining population trend since the 1990s, the city has experienced a steady increase in its elderly population, a demographic group particularly vulnerable to extreme heat during the summer months.<sup>35</sup>

During summer season (July–August) of 2018 in Seoul, the temperature soared to 39.6°C, marking the highest temperature in the 111-year history of meteorological observations. Furthermore, the city experienced 35 heatwave days—defined as instances when the maximum air temperature exceeds 33°C for at least two consecutive days—constituting the highest count since 1943. Additionally, Seoul witnessed 26 tropical nights, a record-breaking period since 1973, during which the temperature remained above 25°C throughout the night. In 2018, the KCDC reported 613 patients suffering from heat-related illnesses in Seoul.<sup>32</sup> This is the highest number of cases recorded between 2017 and 2021, and is approximately 25 times greater than the lowest number of recorded cases in 2020. To obtain a sufficient number of weather stations for accurate air temperature estimations, the spatial extent of the study area included not only the boundaries of Seoul but also its surrounding regions, as depicted in Figure 1B.

#### Data collection for air-temperature estimation

We acquired *in situ* air temperatures from 107 weather stations—1 from ASOS, 41 from automatic weather stations (AWS) operated by the Korea Meteorological Administration (KMA), 2 from forest meteorological stations operated by the National Institute of Forest Science, and 63 weather stations operated by several local governments—located within the study boundary (Figure 1B). To map extreme air temperatures in the summer season, the daily maximum and minimum air temperatures (T<sub>max</sub> and T<sub>min</sub>, respectively) were obtained from June 30 to August 31, 2018.

Multiple datasets from several sources were gathered to produce independent variables (i.e., factors related to air temperature) for air temperature mapping. The elevation was derived from the 90 m resolution Shuttle Radar Topography Mission (SRTM) digital elevation model (DEM). Road data were retrieved from the Open Street Map. We used 250 m resolution Global Human Settlement population and built-up surface (GHS-POP and GHS-BUILT, respectively) for information on the population and impervious surface area. A 250 m resolution mean wind speed for the 10-year period was acquired from Global Wind Atlas.

The clear-sky average daytime LST (DLST) and normalized difference vegetation index (NDVI), built from Landsat 8 satellite data, were used. Launched on February 11, 2013, Landsat 8 crosses the equator at approximately 10 a.m. local time, with a 16-day revisit cycle. The 30 m resolution Landsat 8 satellite image was downloaded from the United States Geological Survey (USGS) Earth Explorer. Among all the available clear-sky (< 1% cloud percentage over the study region) Landsat 8 images, eight scenes from May to September were collected to represent the local climatological data in the warm season (the dates are listed in Table S1). DLST and NDVI were derived from Landsat thermal infrared bands (for DLST) and red and near-infrared bands (for NDVI) using Google Earth Engine.<sup>36</sup> After daily min-max normalization, we averaged the eight DLST and NDVI images to produce local climatology input factors.

Because of the difficulty in obtaining high-resolution (< 250 m) nighttime LST (NLST), the 250 m NLST data produced by Yoo et al. (2022)<sup>37</sup> were used. These 250 m NLST data were downscaled from MODIS Terra daily NLST, which has a 1 km spatial resolution at 10 p.m. local acquisition time. From July to August 2018, we obtained a total of 18 clear-sky NLST data (the dates are listed in Table S2) and averaged them after daily min-max normalization to obtain the NLST as local climatology data.

#### Local climate zone (LCZ)

In this study, an LCZ classification system was employed to analyze the heat distribution derived from interpolated air temperatures and to delineate urban regions for risk-mapping purposes. The LCZ comprises 10 urban types (LCZ1-10) and 7 natural types (LCZA-G),<sup>38</sup> and the full name of each LCZ class is shown in Figure S4. We used Seoul's LCZ map with 50 m resolution, which was produced from multiple sources, such as Sentinel-2A reflectance, Landsat 8 LST, and building datasets based on the convolutional neural networks (CNNs) classifier by Yoo et al. (2020).<sup>28</sup> Although the LCZ map was produced using satellite data obtained in May 2019, it was assumed that there were no significant LCZ type changes in 2018 or 2019. Of the 17 standard LCZ classes, 11, including 7 urban types (LCZ1–6 and 8) and 4 natural types (LCZA, B, D, and G), appeared in Seoul (Figure 1B).

#### De facto and de jure population data

The *de facto* population of Seoul was estimated using public big data from the Seoul Metropolitan Government and telecommunication signals from the Korea Telecom (KT) mobile company. KT is a major telecommunications company, holding a 26.01% share of the market in South Korea as of January 2018. The *de facto* population data were produced based on the long-term evolution (LTE) signal. The LTE signal is collected from the nearest base transceiver station approximately every five minutes when the cellular data is "ON," regardless of cellphone usage. This LTE-based measurement method solves the limitation of irregular collection in the call detail records (CDR)-based measurement method, which collects call and text message signals only when they are in use.<sup>39</sup> The limitations of reducing the generation of signals at night and the deviation in personal cell phone usage were also resolved. This LTE-based *de facto* population estimation is the first of its kind and can expand the total population of an area of interest using the market share of telecommunications.

The *de facto* population is based on hourly measurements, and the region covers 19,153 *Jipgaegu*, the minimum statistical zone unit established by Statistics Korea to measure and provide statistical information. The *de facto* population data for *dong* and *gu*, which are hierarchically at a higher level than *Jipgaegu*, were generated by aggregating the affiliated *Jipgaegu* data. A detailed procedure for estimating the *de facto* population is provided in the Supplementary Information.

Data on the *de jure* population, the elderly living alone, the disabled, and recipients of the National Basic Livelihood Security system used in this study were obtained from the Seoul Statistical Information System. The *de jure* population included the number of Seoul citizens and foreigners living in Seoul under the Korean Resident Registration Act. Data on the population of elderly people living alone were provided,

classified by sex, for people over the age of 65 years living alone in Seoul. The population of disabled people represents the number of people with disabilities registered in autonomous districts, according to the Welfare of Persons with Disabilities Act. The population of recipients of the national basic livelihood security system is the number by autonomous district of people who cannot maintain living payment under the National Basic Livelihood Security Act. The *de jure* population data are renewed quarterly, whereas the data on the other populations are renewed annually by the *dong* unit. In this study, we used the *de jure* population data released for the summer quarter of 2018, whereas for the other populations, we used the figures released as 2018 statistical data.

### Heat-related illness data

The heat-related illness data are provided by the KCDC's integrated disease and health management system.<sup>32,40</sup> These statistics are the result of monitoring the occurrence of heat-related illnesses such as heat stroke, heat exhaustion, heat cramps, heat fainting, heat edema, and estimated heat-related disease due to heatwaves in the summer, counted as reports from approximately 500 emergency room-operating medical institutions nationwide. The heat-related illness data in Seoul were produced from reports of visits to emergency rooms by patients with thermal diseases at sixty-seven emergency rooms at Seoul medical institutions. The period for collecting and releasing data was daily, from 20 May to 30 September. We used the heat-related illness monitoring-system data from a total of twenty-five *gu* units in Seoul from July to August 2018.

### Heat risk mapping framework

The overall procedure of the proposed framework for daily heat risk mapping is shown in Figure S5. First, 250 m spatial resolution daily Tmax and Tmin were produced using a stacking ensemble machine learning spatial modeling technique. Daily heat hazard maps were then produced by averaging the two-day (i.e., consecutive days) cumulative Tmax (for daytime) and Tmin (for nighttime) only for the areas of the urban-type LCZ in each administrative *dong*. Exposure maps were produced by dividing the actual population (3 p.m. during the day and 6 a.m. at night) by the area of the urban LCZ at the administrative *dong* levels. Vulnerability maps were produced through factor analysis using multiple heat vulnerability indicators. Finally, daily heat risk maps were constructed for daytime and nighttime by combining daily hazard, exposure, and vulnerability, and the validation was performed using heat-related illness data.

### Air temperature modeling and analysis

Daily Tmax and Tmin maps were produced using machine learning techniques. *In situ* Tmax and Tmin from the weather stations were used as dependent variables (see the weather stations in Figure 1). A total of 12 input variables known to be significant when modeling urban air temperature were selected.<sup>14,41</sup> (Table S3). The input variables were categorized as topographical (DEM and Slope), urbanization characteristic (Pop, Built, and Road), coordinate (Lat, Lon, and DistC), and climatological (DLST, NLST, NDVI, and Wind) data. Based on the density of the weather stations (the calculation method is suggested by Nichol and Wong<sup>42</sup>) and the spatial resolution of the input data, the spatial scale for the output grids of Tmax and Tmin was determined to be 250 m. DEM, DLST, and NDVI were thus mean aggregated to a resolution of 250 m. The slope was calculated using DEM. Road density (called Road) at 250 m resolution was obtained by line density using the OpenStreetMap (OSM) road shapefile. Generally, temperatures in cities tend to be higher closer to city centers. Using Built as a weight field, the distance from the built-up weighted center (DistC) of the study area was calculated for each 250 m resolution grid. As latitude (Lat) and longitude (Lon) have underlying effects on air temperature, they were also produced at a resolution of 250 m.

To model the air temperatures, this study used stacking ensemble machine learning based on a two-layer machine-learning structure (Figure S6). The first layer consisted of several single models. The single models used in this study are recommended for different algorithms.<sup>43</sup> We included four different single algorithms: support vector regression (SVR), multi-linear regression (MLR), local linear forest (LLF), and cokriging.<sup>44–46</sup> Cokriging is a geostatistical approach based on spatial autocorrelation that combines one or more covariates to predict the target value of an unsampled location using known samples. For cokriging in this study, DEM was chosen as a covariable because elevation is closely associated with air temperature.<sup>41</sup> Because several input variables (e.g., DEM, DLST, and NLST) have linear relationships with the target air temperatures, we selected MLR, LLF, and SVR, where linearity could be considered in the modeling (i.e., a local linear adjustment in LLF and using the linear kernel in SVR). In the second layer, SVR was used as the meta model. Descriptions of cokriging, MLR, SVR, LLF, and stacking ensemble machine learning used are presented in the Supplementary Information.

Spatial modeling was performed daily from June 30 to August 31, 2018, and leave-one-station-out cross-validation (LOSOCV) was conducted to identify the performance of each model. The correlation coefficient (R), root mean square error (RMSE), and mean absolute error (MAE) were used to assess the accuracy. In addition, the spatial distributions of Tmax and Tmin were analyzed based on each LCZ class to identify the differences between the thermal patterns.

### Mapping hazard and exposure

The interpolated air temperatures and LCZ were used to map daily heat hazards. To reflect the heat frequency, we produced two-day cumulative (i.e., consecutive days) air temperatures.<sup>47</sup> The cumulative Tmax and Tmin were then averaged for each of the 424 administrative *dongs* in Seoul to map the daytime and nighttime hazards. As it is most meaningful to focus on areas where people are densely located, the temperatures of the urban-type LCZs (LCZs 1–6 and 8) were selectively averaged. The daily hazard maps for daytime and nighttime at the administrative-*dong* level were min-max normalized based on all values from July to August 2018.

Population density is the predominant indicator for exposure.<sup>10,17</sup> To map the daily heat exposure, we divided the *de facto* population of each *dong* by the total areas of the urban-type LCZs (LCZ 1–6 and 8). For daytime and nighttime exposures, the *de facto* population figures at 3:00 p.m. and 6:00 a.m., respectively, were used. These two hours were selected because they are close to the *T*<sub>max</sub> and *T*<sub>min</sub> times. To compare the distributions of the *de facto* and *de jure* populations, we also produced an exposure map using the *de jure* population data from 2018. As the *de jure* population figure does not distinguish between day and night, an exposure map was generated for 2018. All exposure maps were min-max normalized based on all the values for the period July–August, 2018.

### Mapping vulnerability

Thermal vulnerability greatly depends on demographic and socioeconomic conditions. Some demographic and socioeconomic characteristics were related to the inability to withstand extreme heat. Eight indicators related to heat vulnerability were obtained based on a literature review<sup>48–52</sup> and the availability of the Seoul database (Figure 1). Here, *de facto* population data at 3:00 p.m. and at 6:00 a.m. were used as indicators of daytime and nighttime vulnerability, respectively. Eight indicators (1–8) are used. Four of them (1–4) were based on the *de facto* population. For indicators 1–2, we used the percentages of males and females aged > 50 years. There was a sharp increase in heat-related illnesses in the population aged > 50 years, as reported to the KCDC (2018).<sup>32</sup> For indicators 3–4, the ratios of the *de facto* and *de jure* population figures for the elderly (over 65 years) for males and females were used. We assumed that a higher value of this ratio was associated with a greater possibility of physical exposure to heat owing to the different areas of residence and activity.<sup>53</sup> The other four indicators (5–8), as key sources of social isolation, were obtained from *de jure* population data, as they could not be derived from *de facto* population data. For indicators 5–7, the percentages of elderly males and females living alone and those with disabilities were used. These groups lack opportunities to obtain assistance when extreme heat occurs. For indicator 8, we considered the percentage of basic livelihood recipients. This group is poorly prepared for extreme heat.

This study used principal component analysis (PCA) to produce daytime and nighttime heat vulnerability maps. PCA has been widely used in vulnerability mapping because it can reduce the number of correlated variables to a small dimension, helping to identify the latent meanings between the variances of uncorrelated data.<sup>48,54,55</sup> PCA was conducted using a covariance matrix in which the elements were normalized and standardized, considering that each variable had a different variance and unit. Kaiser-Meyer-Olkin and Bartlett’s tests were then performed to select suitable principal components (PCs) with eigenvalues greater than 1.<sup>56</sup> Varimax rotation was performed to interpret and maximize the selected PCs’ loadings. These rotated PCs were then weighted by the variance explained by each component and aggregated to produce a combined PC score (i.e., a variance-weighted approach<sup>57</sup>), which represents heat vulnerability at the administrative *dong* level. The resulting vulnerability maps were min-max normalized for each date.

### Heat risk mapping and validation

Daily daytime and nighttime heat risks were mapped by combining the three component layers—hazard, exposure, vulnerability—in equal weights, because there is no standard regarding which component is more important than the others.<sup>10,58</sup> When validating the heat risk map, the administrative *dong* level heat risk measures were mean-aggregated to the *gu* level to match the spatial scale of heat risks to the heat-related illness data. Validation was implemented on a monthly time scale because the sample size (i.e., heat-related illness) was very small on a daily scale. Therefore, the aggregated daily heat risk measure was averaged for July–August 2018. The number of heat-related illnesses for each *gu* was also averaged from July to August. We divided this average number of heat-related illnesses by the *de jure* population figure to produce a heat-related illness ratio (%) for each *gu*.<sup>11</sup> The spatial correlation between the heat risk measure and the heat-related illness ratio for 25 *gu* in Seoul was calculated to validate the proposed framework.

We also compared the accuracy of the proposed heat risk map with that of another framework that uses only the *de jure* population to calculate exposure and vulnerability (see Figure S7). In addition, temporal validation of the daily heat risk was implemented. First, the three *gu* regions with the highest number of heat-related illnesses in the summer of 2018 were selected. The three *gu* units constituted a relatively sufficient sample size (> 50 cases per year) to show temporal variation. The average value of the number of daily heat-related illness cases for each *gu* and the average value of the daily heat risk were set as thresholds,<sup>59</sup> and classification was performed based on a contingency table (Table S4). The heat risk measures for the three *gu* were evaluated by calculating the probability of detection (POD; Equation 1), false alarm rate (FAR; Equation 2), and critical success index (CSI; Equation 3).

$$POD = \frac{H}{H+M} \quad (\text{Equation 1})$$

$$FAR = \frac{F}{H+F} \quad (\text{Equation 2})$$

$$CSI = \frac{H}{H+M+F} \quad (\text{Equation 3})$$